



Supplement of

Biogeomorphic modeling to assess the resilience of tidal-marsh restoration to sea level rise and sediment supply

Olivier Gourgue et al.

Correspondence to: Olivier Gourgue (ogourgue@gmail.com)

The copyright of individual parts of the supplement might differ from the article licence.

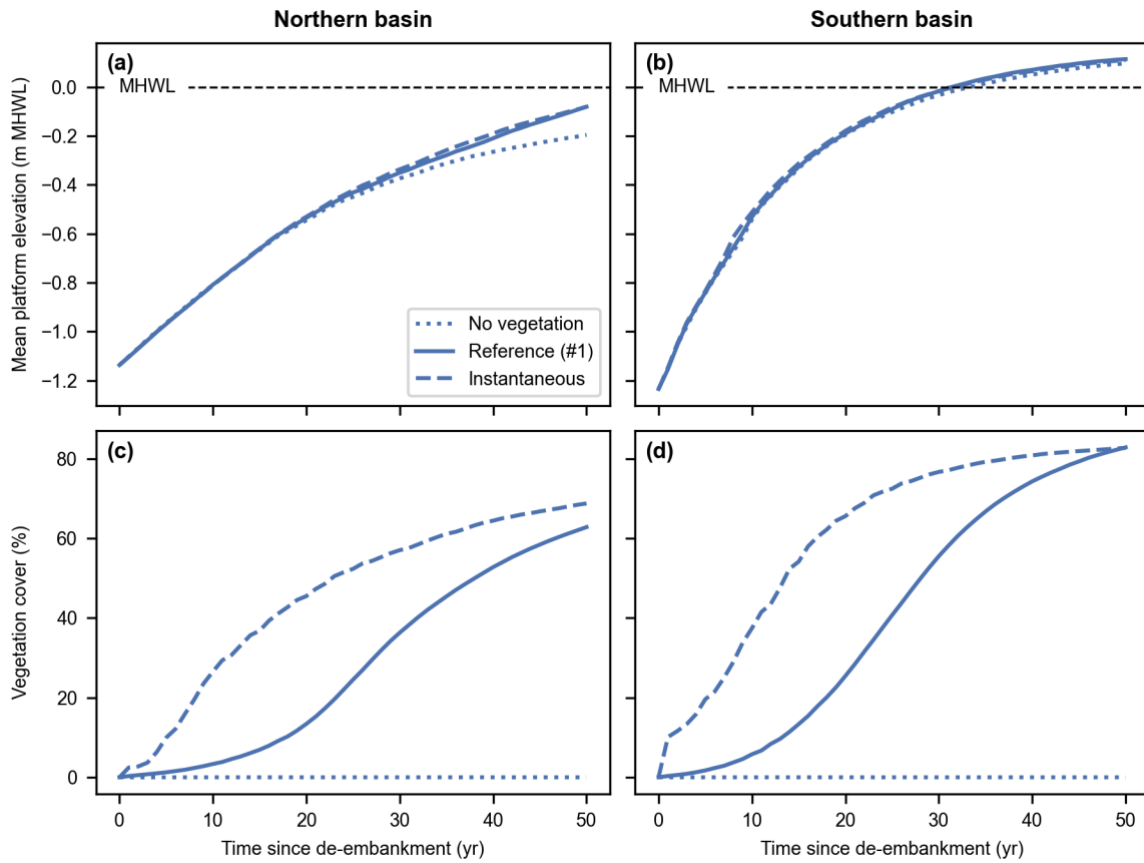


Figure S1: Vegetation dynamics model scenarios (i.e., reference vegetation dynamics and two variants, respectively without vegetation and with instantaneous colonization – Table S1). Evolution of the mean platform elevation with respect to the mean high-water level (MHWL) (a-b) and development of the vegetation cover (c-d) in the Northern (a, c) and Southern basins (b, d).

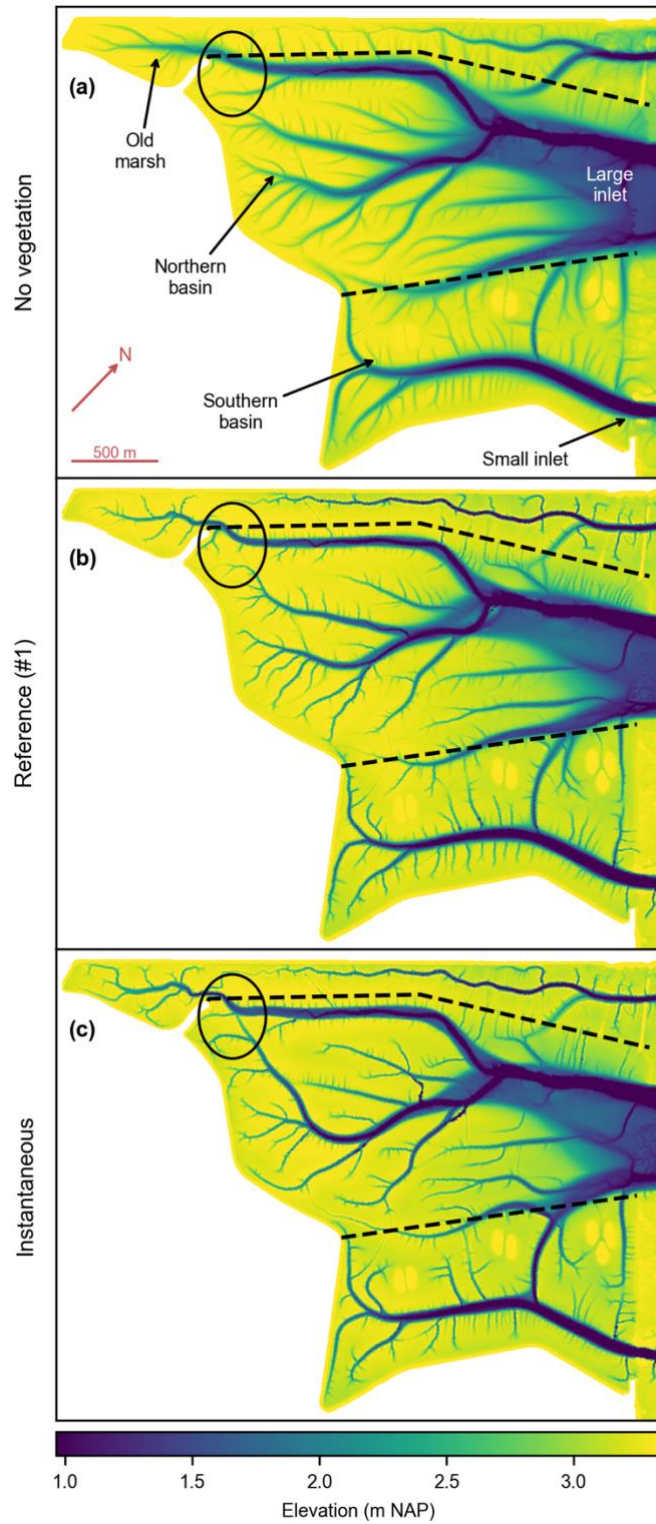


Figure S2: Vegetation dynamics model scenarios (i.e., reference vegetation dynamics (a) and two variants, respectively without vegetation (b) and with instantaneous colonization (c) – Table S1). Bed elevation 50 years after de-embankment. The dashed lines delineate the old marsh, the Northern basin, and the Southern basin. The ellipses emphasize a pre-excavated channel that has disappeared (a-b) or survived (c), depending on the vegetation dynamics. All figures are rotated by 43° clockwise, as compared to Fig. 2c.

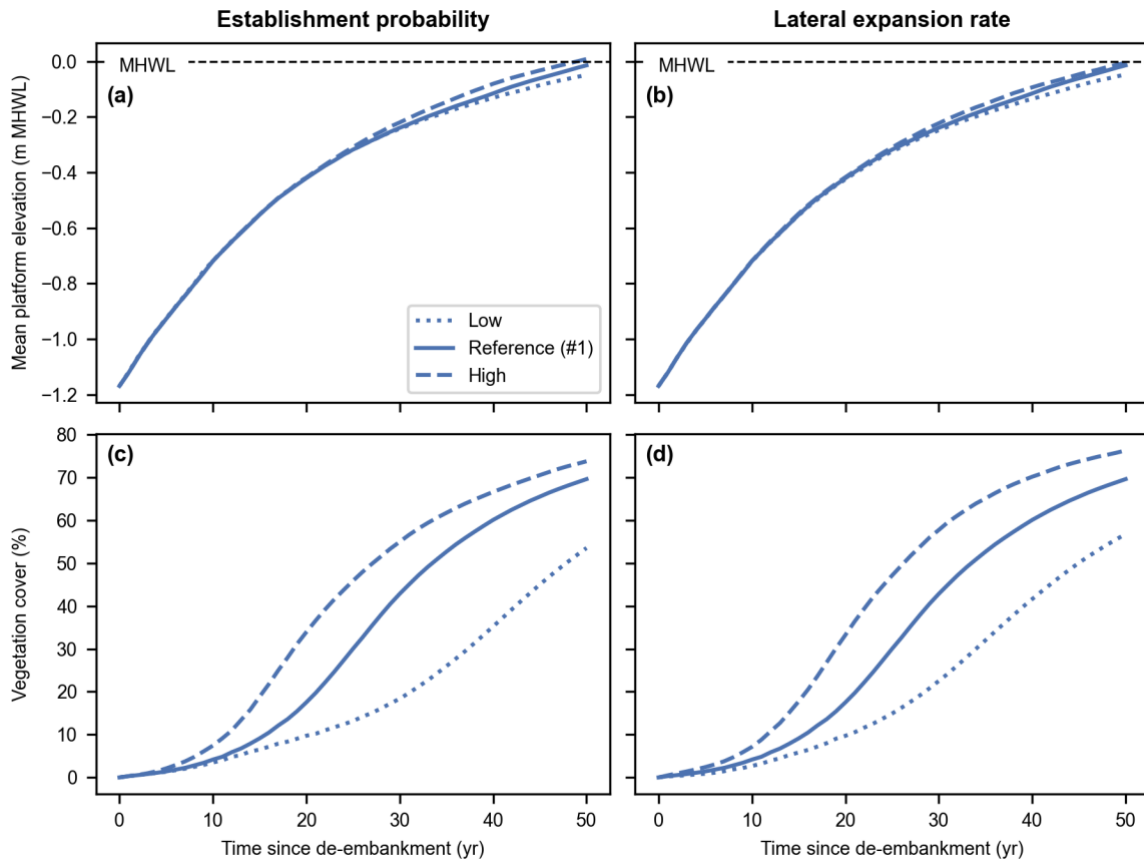


Figure S3: Vegetation input parameter model scenarios (i.e., reference vegetation dynamics and four variants, respectively with low and high establishment probability (a, c), and with low and high lateral expansion rate (b, d) – Table S1). Evolution of the mean platform elevation with respect to the mean high-water level (MHWL) (a-b) and development of the vegetation cover (c-d).

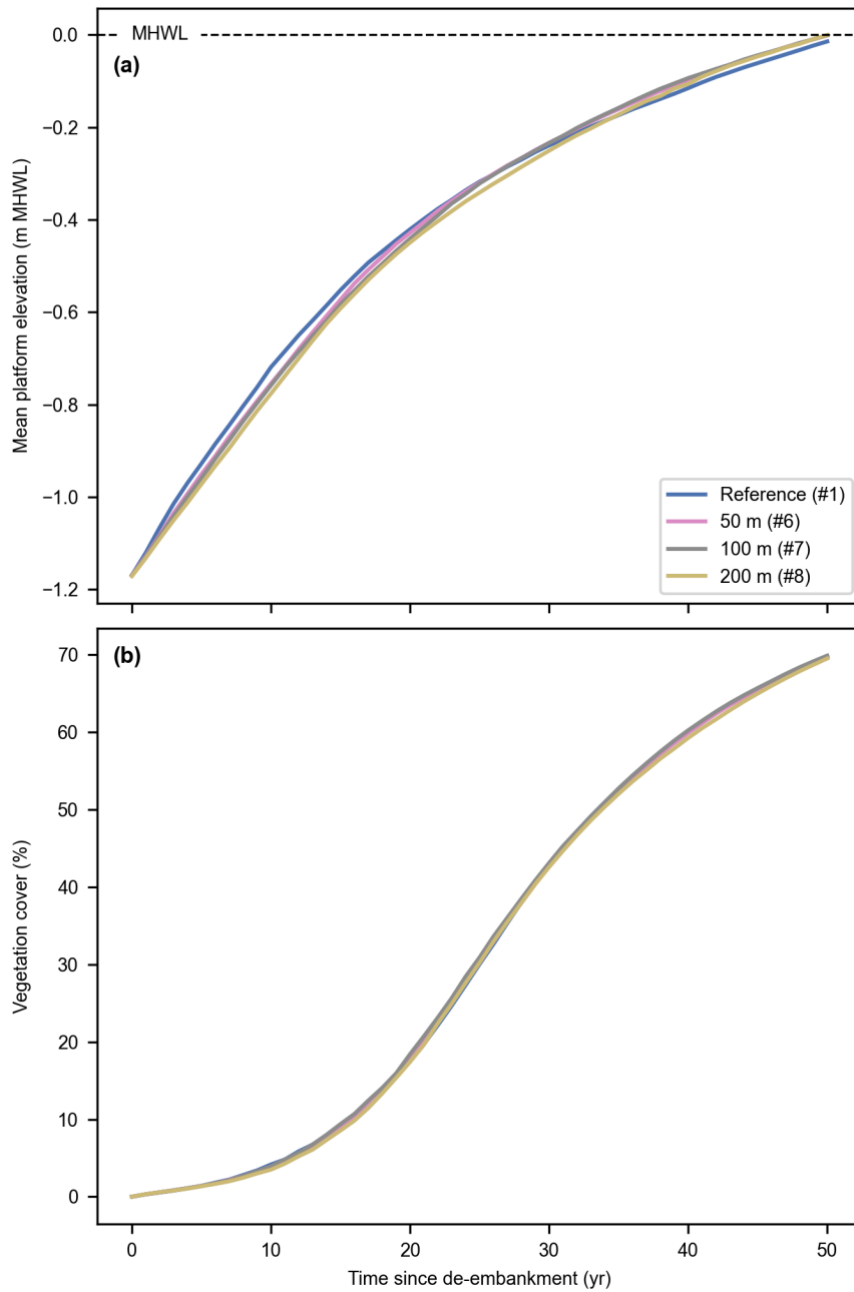


Figure S4: Inlet design model scenarios (i.e., reference design and three alternative designs with small-inlet breach size of respectively 50, 100 and 200 m, and excavated channel – #1, 6-8). Evolution of the mean platform elevation with respect to the mean high-water level (MHWL) (a) and development of the vegetation cover (b) in the Northern and Southern basins combined.

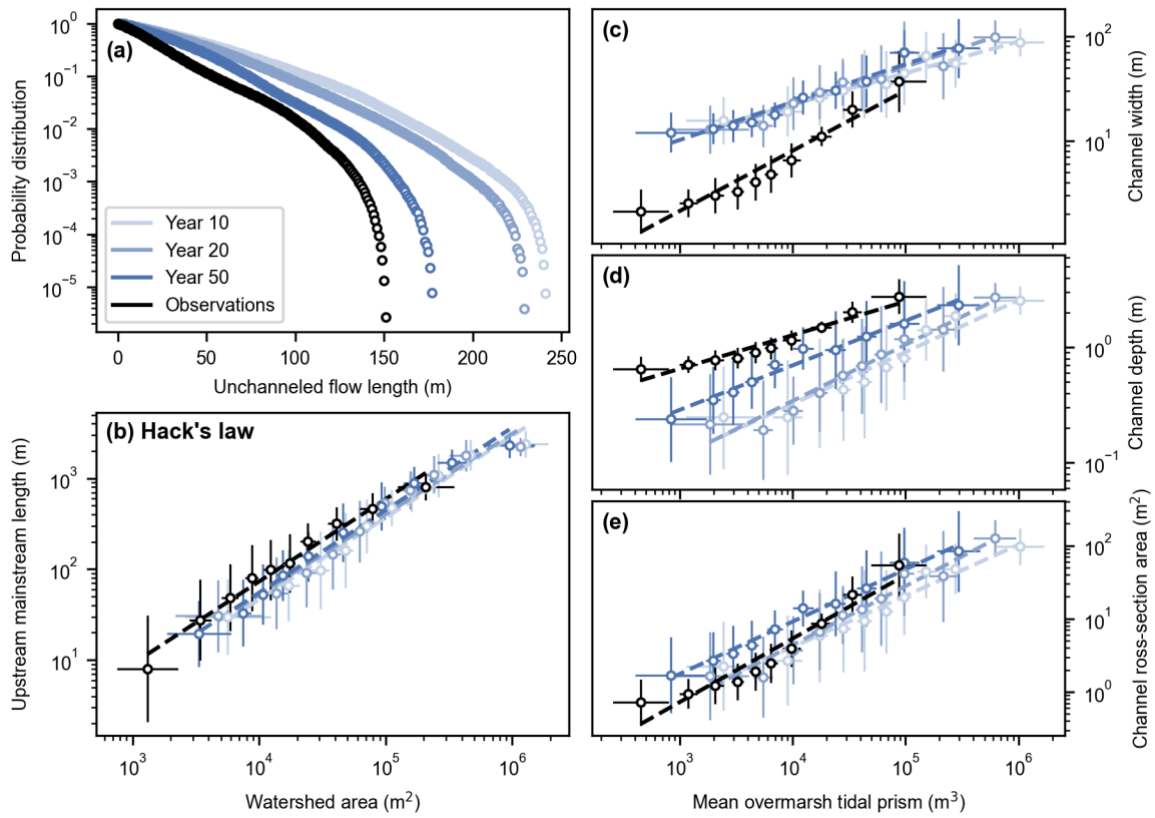


Figure S5: Reference model scenario (#1). Channel geometric properties 10, 20 and 50 years after de-embankment (different shades of blue) compared to observations in an established marsh nearby the study site (black). Probability distribution of the unchanneled flow length (a), upstream mainstream length vs. watershed area (b), and channel width (c), channel depth (d) and channel cross-section area (e) vs. mean overmarsh tidal prism. (b-e) Model results and observations are respectively split into 10 sub-samples of equal size (Sect. 2.4.4). Markers and error bars represent the geometric means and standard deviations of each sub-sample. Dashed lines represent geometric regressions of the geometric means.

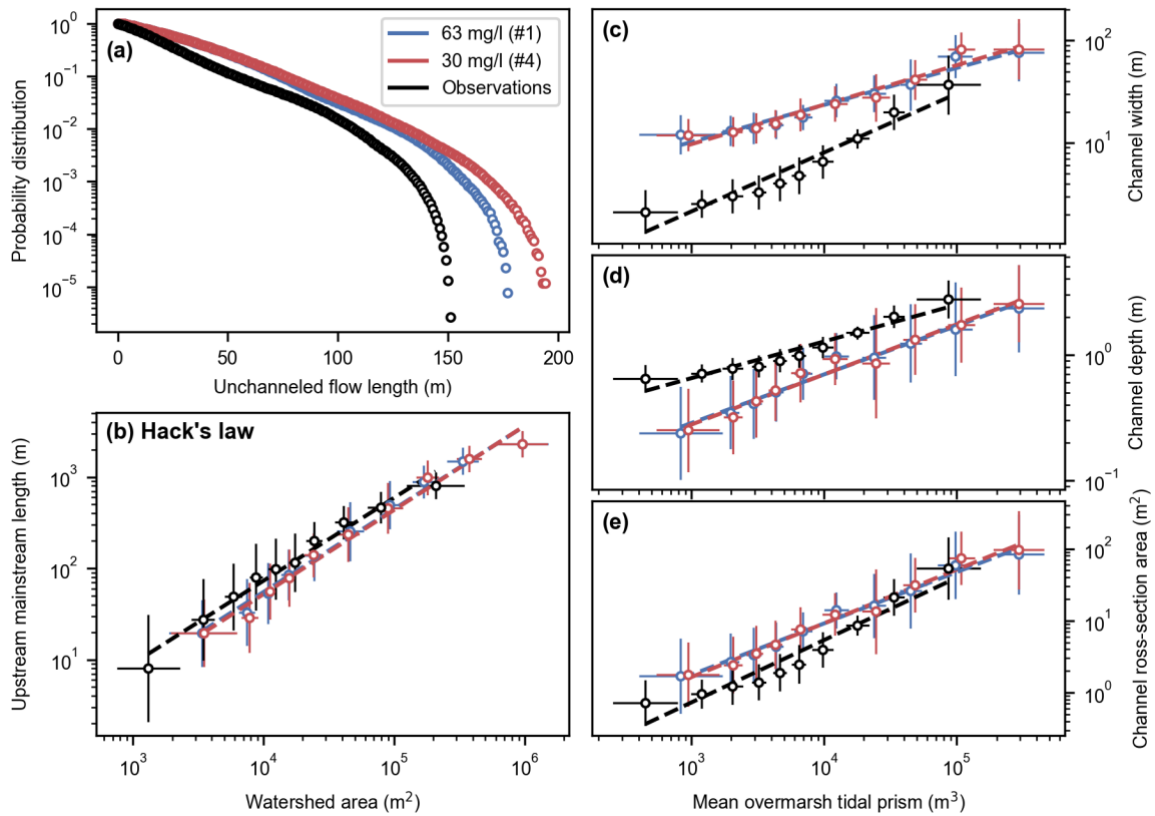


Figure S6: Suspended sediment concentration model scenarios (#1, 4). Channel geometric properties 50 years after de-embankment (blue, red) compared to observations in an established marsh nearby the study site (black). Probability distribution of the unchanneled flow length (a), upstream mainstream length vs. watershed area (b), and channel width (c), channel depth (d) and channel cross-section area (e) vs. mean overmarsh tidal prism. (b-e) Model results and observations are respectively split into 10 sub-samples of equal size (Sect. 2.4.4). Markers and error bars represent the geometric means and standard deviations of each sub-sample. Dashed lines represent geometric regressions of the geometric means.

Table S1: Specifics of the reference model scenario variants used in Figure S1 to Figure S3.

Variant name	Vegetation module parameterizations
No vegetation	No vegetation module.
Instantaneous colonization	Table S5 .
Low establishment probability	Table S4 , but P_2^{est} , P_3^{est} and $P_{2,3}^{suc}$ divided by 10.
High establishment probability	Table S4 , but P_2^{est} , P_3^{est} and $P_{2,3}^{suc}$ multiplied by 10.
Low lateral expansion rate	Table S4 , but R_2^{exp} , $R_3^{exp} = 1$ m/yr.
High lateral expansion rate	Table S4 , but R_2^{exp} , $R_3^{exp} = 5$ m/yr.

Table S2: Coefficients of determination (R^2) of the linear regressions obtained from model results and observations in Fig. 4a and 5, and p -values of the ANCOVA performed to determine whether linear regressions from model results and observations are statistically equal (both p -values must be higher than 0.05). The first p -value determines whether the slopes of the linear regressions are significantly different (if $p < 0.05$) and the second p -value whether their intercepts are significantly different (if $p < 0.05$).

Figure	R^2 (model)	R^2 (observations)	p (slopes)	p (intercepts)
Fig. 4a	0.966	0.987	0.496	0.412
Fig. 5b	0.985	0.977	0.913	0.007
Fig. 5c	0.955	0.929	0.001	< 0.001
Fig. 5d	0.973	0.929	0.056	< 0.001
Fig. 5e	0.985	0.929	0.023	0.004

S1 Biogeomorphic model

We have developed the biogeomorphic modeling framework Demeter to simulate explicitly the feedbacks between hydrodynamics, morphodynamics (Sect. S1.1) and vegetation dynamics (Sect. S1.2). This is a multiscale approach, in which the vegetation dynamics is computed at much finer resolution than the hydro-morphodynamics (Fig. 1), requiring the development of specific multiscale coupling techniques to preserve subgrid-scale heterogeneity while information is exchanged between the hydro-morphodynamic and vegetation modules (Sect. S1.3 and S1.4). The specific setup for our study site is detailed in Sect. S1.5.

S1.1 Telemac (hydro-morphodynamics)

As hydro-morphodynamic module (Fig. 1a), we use the finite element solver suite Telemac (version 7.3.0), and more specifically its modules Telemac-2D for the hydrodynamics and Sisyphe for the sediment transport and the morphodynamics.

Telemac-2d solves the depth-averaged shallow water equations in a two-dimensional horizontal framework (Hervouet, 2007) to simulate fluctuations of the water depth h and the depth-averaged flow velocity \mathbf{u} :

$$\frac{\partial h}{\partial t} + \nabla \cdot (h\mathbf{u}) = 0 \quad (\text{S1})$$

$$\frac{\partial \mathbf{u}}{\partial t} + \mathbf{u} \cdot \nabla \mathbf{u} = -g\nabla\eta + \frac{1}{h}\nabla \cdot (h\nu\nabla\mathbf{u}) - \frac{\boldsymbol{\tau}_b + \boldsymbol{\tau}_v}{\rho h} \quad (\text{S2})$$

where t is the time, ∇ is the spatial differential operator, g is the gravitational acceleration, η is the water surface elevation above the reference level (NAP), ν is the diffusion coefficient, $\boldsymbol{\tau}_b$ is the bed shear stress, $\boldsymbol{\tau}_v$ is the vegetation resistance force per unit horizontal area, and ρ is the water density. The bed shear stress is computed with the Manning formula:

$$\boldsymbol{\tau}_b = \frac{\rho g n^2}{h^{1/3}} \|\mathbf{u}\| \mathbf{u} \quad (\text{S3})$$

where the Manning coefficient n is empirically derived and depends mainly on bed roughness. The vegetation resistance force is modeled as the drag force on a random or staggered array of rigid cylinders with uniform properties (Baptist et al., 2007) and depends on the spatial distribution of vegetation provided by the cellular automaton (Sect. S1.4).

Sisyphe solves the depth-averaged advection-diffusion equation to simulate fluctuations of the depth-averaged suspended sediment concentration C :

$$\frac{\partial hC}{\partial t} + \nabla \cdot (huC) = \nabla \cdot (hv\nabla C) + E - D \quad (S4)$$

where E and D are the rates of sediment erosion and deposition, respectively. The rate of sediment erosion is computed using the equation of [Partheniades \(1965\)](#):

$$E = \begin{cases} M \left(\frac{\|\tau_b\|}{\tau_e} - 1 \right) & \text{if } \|\tau_b\| > \tau_e \\ 0 & \text{otherwise} \end{cases} \quad (S5)$$

where M is the Partheniades constant and τ_e is the critical bed shear stress for sediment erosion. The rate of sediment deposition is computed using the equation of [Einstein and Krone \(1962\)](#):

$$D = w_s C \quad (S6)$$

where w_s is the sediment settling velocity. The existence of a threshold shear stress below which sediments remain in suspension is debated in the literature. Here we follow one of the well-established arguments that such threshold does not exist, and that it rather represents a threshold for erosion of freshly deposited sediments ([Winterwerp, 2007](#)). This approach agrees with field observations in the Chesapeake Bay ([Sanford and Halka, 1993](#)) and is often adopted in recent biogeomorphic models (e.g., [Adams et al., 2016](#); [Bryan et al., 2017](#); [Mariotti, 2018](#); [Zhang et al., 2019](#); [Brückner et al., 2020](#)).

The evolution of the bed is computed as follows:

$$\frac{\partial b}{\partial t} = \alpha \frac{D - E}{\rho_s} \quad (S7)$$

where b is the bed surface elevation above the reference level (NAP), α is the morphological acceleration factor ([Sect. 2.1](#)) and ρ_s is the sediment dry bulk density. The bed is composed of two layers: the fresh layer at the surface and the compacted layer underneath. Their evolution obeys the following rules: (i) each layer is characterized by different values of τ_e and ρ_s , (ii) erosion of the compacted layer only occurs where and when the fresh layer is locally empty, (iii) deposition only occurs on the fresh layer, and (iv) there is no sediment flux between the two layers.

S1.2 Cellular automaton (vegetation dynamics)

As vegetation module, we use the cellular automaton implemented in Demeter. A cellular automaton consists of a regular grid of cells, each one with a finite number of states (here, either bare or one of the considered vegetation species). Cells can change their state in

discrete time steps, depending on their neighborhood state and a set of simple stochastic transition rules (Balzter et al., 1998).

Our cellular automaton is implemented as a hierarchical model, where higher-rank species are stronger competitors able to outcompete lower-rank species. In our model, higher-rank species can displace lower-rank species, but not the other way around. Lower-rank species can only colonize after higher-rank species have died off. On the long term, high-rank species will therefore always outcompete lower-rank species in their own niche.

S1.2.1 Establishment

Establishment is the transition from bare state 0 to any vegetated state i . The probability of establishment p_i^{est} for species i is evaluated as:

$$p_i^{est} = P_i^{est} \prod_k f_k \quad (S8)$$

where P_i^{est} is the background probability of establishment for species i , and f_k are stress functions of the environmental variables (Sect. S1.2.5).

S1.2.2 Succession

Succession is the transition from any vegetated state i to another vegetated state $j > i$ (e.g., from pioneer to climax vegetation). The probability of succession $p_{i,j}^{suc}$ from species i to j is evaluated as:

$$p_{i,j}^{suc} = P_{i,j}^{suc} \prod_k f_k \quad (S9)$$

where $P_{i,j}^{suc}$ is the background probability of succession from species i to j .

S1.2.3 Stress-related die-off

Stress-related die-off (or simply die-off) is the transition from any vegetated state i to bare state 0 due to environmental stress. The probability of die-off p_i^{die} for species i is evaluated as follows:

$$p_i^{die} = 1 - \prod_k (1 - f_k) \quad (S10)$$

S1.2.4 Annual die-off

Annual die-off is the transition from any vegetated state i to bare state 0 due to the natural cycle of annual species. The probability of annual die-off p_i^{ann} for species i is evaluated as follows:

$$p_i^{ann} = P_i^{ann} \quad (S11)$$

where P_i^{ann} is the background probability of annual die-off for species i .

S1.2.5 Stress functions

Stress functions (Sect. S1.2.1 to S1.2.3) can be of two shapes. When vegetation is only affected at high (resp. low) values of an environmental stressor, and not below (resp. above) a certain threshold, we use the Hill function, which varies from 0 to 1 following:

$$f_H(x; H, N) = \frac{x^N}{H^N + x^N} \quad (S12)$$

where x is the environmental variable, H is the threshold around which the transition from 0 to 1 occurs, and N is a parameter that controls the shape of the function. The function decreases from 1 to 0 if $N < 0$ and increases from 0 to 1 if $N > 0$. The transition from 0 to 1 becomes steeper for increasing $|N|$.

When the range of optimal conditions is confined between a low and a high threshold value, we use the Brière function:

$$f_B(x; X_0, X_1) = \max\left(\frac{x(x - X_0)(X_1 - x)}{c}, 0\right) \quad (S13)$$

where X_0 and X_1 are the low and high thresholds, respectively, and c is a coefficient used to rescale the function, so that its maximum value is 1:

$$c = x_{opt}(x_{opt} - X_0)(X_1 - x_{opt}) \quad (S14)$$

$$x_{opt} = \frac{1}{3}\left(X_0 + X_1\sqrt{X_1^2 - X_0X_1 + X_0^2}\right) \quad (S15)$$

The different environmental variables used for the stress functions are the hydroperiod, the bed elevation gain and loss, and the binned shear stress (Sect. S1.3.1).

S1.2.6 Lateral expansion

Lateral expansion is the transition from any state i (bare or vegetated) to any vegetated state $j > i$ resulting from the presence of at least one neighboring cell of state j . The recruitment process is here quite different than for the other processes. It is defined by the mean expansion rate R_i^{exp} , which determines the number of iterations N_{exp} of the cellular automaton. For each iteration, the probability of recruitment by lateral expansion p_i^{exp} is

$$p_i^{exp} = \frac{R_i^{exp}}{N_{exp}\Delta x} \quad (S16)$$

where Δx is the grid resolution of the cellular automaton. With this stochastic approach, even though the mean expansion rate is constant, the actual expansion rate varies in space and time. The number of iterations is determined so that

$$R_{max} > R_i^{exp} + 2\sigma^2 \quad (S17)$$

where the maximum expansion rate R_{max} and the variance of the expansion rate σ^2 are calculated as follows:

$$R_{max} = N_{exp}\Delta x \quad (S18)$$

$$\sigma^2 = N_{exp}p_i^{exp}(1 - p_i^{exp})\Delta x = R_i^{exp} \left(1 - \frac{R_i^{exp}}{N_{exp}\Delta x} \right) \quad (S19)$$

As each species can have a different mean expansion rate, and hence a different number of iterations, we use the highest number of iterations among all species.

S1.2.7 Computational sequence

The different transition rules of the cellular automaton are scheduled as follows:

1. Annual die-off is applied for each annual species in one single iteration.
2. Establishment, succession, and lateral expansion are applied for all species in an iterative process. The number of iterations is determined based on the mean expansion rates (Sect. S1.2.6). For each iteration, the probabilities of establishment, succession and lateral expansion are rescaled as follows:

$$p_i^{est} \leftarrow 1 - (1 - p_i^{est})^{N_{exp}} \quad (S20)$$

$$p_{i,j}^{suc} \leftarrow 1 - (1 - p_{i,j}^{suc})^{N_{exp}} \quad (S21)$$

$$p_i^{exp} \leftarrow p_i^{exp} \frac{N_{nb}}{4} \quad (S22)$$

where N_{nb} is the number of neighboring cells vegetated with the same species i at the previous iteration. We use a factor $\frac{1}{4}$ in Eq. S22, so that the rescaling factor $\frac{N_{nb}}{4}$ is 1 on average.

3. Stress-related die-off is then applied in one single iteration.

S1.3 Coupling Telemac to cellular automaton

S1.3.1 Environmental variables

The hydroperiod T_H is the percentage of time during which a Telemac grid node is flooded (i.e., the water depth higher than 0.1 m) between two cellular automaton calls. It varies between 0 (never flooded) and 1 (always flooded).

The bed elevation change Δb is the difference between the final and initial bed elevations between two cellular automaton calls. The bed elevation gain Δb_+ and the bed elevation loss Δb_- are calculated as:

$$\Delta b_+ = \max(\Delta b, 0) \quad (S23)$$

$$\Delta b_- = \max(-\Delta b, 0) \quad (S24)$$

The binned shear stress is calculated by classifying flow directions into 8 directional bins (45° each) occurring between two cellular automaton calls. The relative binned time T^i , the binned shear stress $\bar{\tau}_b^i$, and the binned water depth \bar{h}^i are respectively the percentage of time, the mean bed shear stress, and the mean water depth when the flow is oriented in the i^{th} bin. As bed shear stress and flow directions are especially relevant above certain thresholds of the water depth and the bed shear stress, these binned variables only account for situations when the water depth is higher than 0.1 m and the bed shear stress is higher than 0.1 N m⁻².

The mean water depth \bar{h} between two cellular automaton calls is calculated for situations when the water depth is higher than 0.1 m.

S1.3.2 Spatial refinement

We use a linear interpolation to spatially refine the hydroperiod, and the bed elevation gain and loss from the Telemac grid to the cellular automaton grid.

We use the concepts of Voronoi neighborhood to spatially refine the relative binned time and the binned water depth. Each cellular automaton grid cell is associated with its closest Telemac grid node. The Voronoi neighborhood of a Telemac grid node is the ensemble of all associated cellular automaton grid cells. Here, the relative binned time and the binned water depth of a Telemac grid node are passed to all cellular automaton grid cells of its Voronoi neighborhood.

For the binned shear stress, we use a convolution method that allows to account for interactions between flow and subgrid-scale vegetation patterns (Gourgue et al., 2021). Practically, we first calculate the binned velocity \bar{u}^i on the Telemac grid as follows:

$$\bar{u}^i = \left(\frac{\bar{\tau}_b^i (\bar{h}^i)^{1/3}}{\rho g n^2} \right)^{1/2} \quad (S25)$$

Then, we use a convolution method (Gourgue et al., 2021) to spatially refine the mean binned velocity from the Telemac grid to the cellular automaton grid. Finally, we calculate the binned shear stress on the Telemac grid as follows:

$$\bar{\tau}_b^i = \frac{\rho g n^2}{(\bar{h}^i)^{1/3}} (\bar{u}^i)^2 \quad (S26)$$

S1.3.3 Stress function of the binned shear stress

A stress function of the binned shear stress (typically using the Hill function) requires a specific treatment to combine all its components. It is calculated as follows:

$$f = 1 - \prod_{i=1}^8 \left(1 - f_H(\bar{\tau}_b^i; H, N)\right)^{T^i} \quad (S27)$$

S1.4 Coupling cellular automaton to Telemac

S1.4.1 Vegetation resistance force

For the vegetation resistance force per unit horizontal area τ_v in Eq. S2 of the hydro-morphodynamic module, we use the approach introduced by Baptist et al. (2007), which considers plants as rigid cylinders with uniform morphological properties (i.e., stem density, diameter and height). As compared to the original method, we here neglect the extra term depending on the ratio between water depth and plant height, and we combine linearly the separate effect of each plant species:

$$\tau_v = \frac{1}{2} \rho \beta \left(\sum_i C_{Di} \gamma_i m_i d_i \min(h, k_i) \right) \|\mathbf{u}\| \mathbf{u} \quad (S28)$$

where β is the transmittance coefficient (Sec. S1.4.2), and C_{Di} , γ_i , m_i , d_i and k_i are respectively the bulk drag coefficient (Baptist et al., 2007), the vegetation cover (Sec. S1.4.2), the stem density, the stem diameter and the stem height of species i .

S1.4.2 Spatial coarsening

The vegetation cover γ_i of the species i is the percentage of cellular automaton cells of state i within the Voronoi neighborhood of a Telemac grid node (Sec. S1.3.2). It varies between 0 (not covered by species i) and 1 (fully covered by species i). The sum of all vegetation covers also varies between 0 (bare) and 1 (fully covered by vegetation).

The transmittance coefficient β accounts for the spatial heterogeneity of the vegetation distribution at the subgrid scale (i.e., within a Voronoi neighborhood). In general,

hydrodynamic models assume a uniform spatial distribution at the subgrid scale (here, $\beta = 1$), which leads to considerable overestimation of the flow resistance if the vegetation presents clustered patterns at the subgrid scale (Gourgue et al, 2019). The method to compute the transmittance coefficient β builds on the similarity between the Chézy formula in fluid dynamics and Ohm's law in electricity. Taking the analogy further, we recalculate the coarse-scale hydraulic roughness just as the total resistance of an electronic circuit that combines resistors (equivalent to cellular automaton cells in our analogy) connected in series (along-flow) and in parallel (across-flow). The transmittance coefficient β is calculated at the end of a cellular automaton call. It varies between 0 and 1 and it has different values depending on the flow direction (Gourgue et al, 2019).

S1.5 Study site setup

S1.5.1 Hydro-morphodynamic module

The initial bed elevation is based on the project design (Sec. 2.2 and Fig. 2) and Lidar data before de-embankment. The bed is initially exclusively composed of a compacted layer. Tides are imposed into the system by defining water levels and flow velocities at the open boundary between the study site and the Scheldt Estuary, which is here approximately the isobath 5 m below the mean low water level. These boundary conditions are provided by a 3D hydrodynamic model of the estuary, which has been calibrated for a spring-neap cycle by comparison with measurements of water levels, flow velocities and water discharges (Maximova et al., 2014). To reduce the computational time, we do not simulate the entire range of tidal conditions of a full spring-neap cycle. Instead, we only select four different semi-diurnal tidal cycles from the estuarine model, which are representative of the standard range of tidal conditions that can be observed in that area. With high water levels of 2.05, 2.55, 2.87 and 3.25 m NAP, the selected tidal cycles have a frequency distribution of respectively 14.6%, 27.4%, 32.3% and 25.7%, as compared to historical measurements during the period 2007-2017. These frequency distributions are then used to determine the morphological acceleration factor α used for each semi-diurnal tidal cycle (Sec. 2.1). We simulate the impact of sea level rise by lowering the bed elevation every year by a value corresponding to the yearly increase of mean sea level. The suspended sediment concentration at the open boundary is constant and determined based on reported measurements (Vandenbruwaene et al., 2014; Sec. S2). All parameter values used in the hydro-morphodynamic module are

based on previous studies in the same restored tidal marsh area ([Maximova et al., 2014](#); [Zhou et al., 2016](#)), the Scheldt Estuary ([van Leussen, 1999](#); [Van de Broek et al., 2018](#)) and other intertidal environments ([D'Alpaos et al., 2021](#)). They are summarized in Table S3. The suspended sediment concentration at the open boundary and the rate of sea level rise vary according to model scenarios ([Table 1](#)).

Table S3: Hydro-morphodynamic module parameter values.

Parameter	Symbol	Value	Reference
Gravitational acceleration	g	9.81 m s ⁻²	Standard
Diffusion coefficient	ν	1 m ² s ⁻¹	Calibration
Water density	ρ	1000 kg m ⁻³	Standard
Manning coefficient	n	0.021 s m ^{-1/3}	Maximova et al., 2014
Partheniades constant	M	10 ⁻⁴ kg m ² s ⁻¹	D'Alpaos et al., 2012; Zhou et al., 2016
Critical bed erosion shear stress	τ_e	0.5 N m ⁻² (fresh layer)	Zhou et al., 2016
		0.8 N m ⁻² (compacted layer)	Zhou et al., 2016; D'Alpaos et al., 2012
Settling velocity	w_s	1 mm s ⁻¹	van Leussen, 1999
Morphological acceleration factor	α	103 (neap tide)	Sec. 2.1 and S1.5
		193.5 (mid-neap tide)	
		228 (mid-spring tide)	
		181.5 (spring tide)	
Dry bulk density	ρ_s	500 kg m ⁻³ (fresh layer)	Van de Broek et al., 2018
		1500 kg m ⁻³ (compacted layer)	
Bulk drag coefficient	C_D	2 (pioneer marsh)	Calibration (Gourgue et al., 2021) with flume measurements (Schwarz et al., 2015)
		1 (middle marsh)	
		5 (high marsh)	
Stem density	m	214 m ⁻² (pioneer marsh)	Field observations
		338 m ⁻² (middle marsh)	
		298 m ⁻² (high marsh)	
Stem diameter	d	12 mm (pioneer marsh)	Field observations
		6.8 mm (middle marsh)	
		5.98 mm (high marsh)	
Stem height	k	1 m (pioneer marsh)	Field observations
		1.03 m (middle marsh)	
		2.36 m (high marsh)	

S1.5.2 Vegetation module

The study site is in the oligohaline zone (0.5 – 5 PSU) where *Aster tripolium* is often observed as the pioneer species, and *Scirpus maritimus* and *Phragmites australis* in the marsh interior (Van Braeckel et al., 2008). Their expected encroachment in our study site is further supported by the results of transplantation experiments carried out in nearby tidal marshes. *Aster tripolium* is an annual species, which can be found as lower pioneer in calm areas and along creek edges. It colonizes the tidal flats and creek levees every year from seeds, as randomly scattered high density clusters on tidal flats. Although it is regarded as an annual species, part of the established plants can survive and develop for another year. *Scirpus maritimus* is the dominant perennial species from the low pioneer zone into the middle marsh zone. It is even the only species present in the pioneer zone in several tidal marshes close to the study site. The main mode of colonization on bare tidal flats is via lateral spread of rhizomes (Silinski et al., 2016). *Phragmites australis* is the dominant species in the high marsh zone. It can form large stands from the high pioneer zone up to the supratidal zone, but it is mostly found above *Scirpus maritimus* in the middle and high marsh zone. Most seedling establishment occurs within already established vegetation, but very rarely on bare tidal flats, except for the highest areas. Once established, it can often outcompete *Scirpus maritimus* and colonize vegetated areas by lateral expansion via rhizomes, resulting in clearly visible circular patches within *Scirpus maritimus* marshes.

The initial vegetation distribution is based on aerial pictures before de-embankment. Marshes that will be excavated and farmland are considered as unvegetated. Parameterization of the different stress functions (Sec. S1.2.5) is based on field and flume experiments, remote sensing, literature data and model calibration (Table S4-Table S5).

Table S4: Vegetation module parameterizations (reference vegetation dynamics, used in model scenarios #1-8).

Process	Contribution	Reference
<i>Aster tripolium</i> (species 1, pioneer marsh)		
Establishment (Eq. S8)	$P_1^{est} = 0.2$	Calibration
	$f_B(T_H; 0.039, 0.1134)$	Field experiments; Silinski et al., 2016
	$f_H(\Delta b_+; 0.03 \text{ m}, -2.37)$ $f_H(\Delta b_-; 0.001 \text{ m}, -4)$	Bouma et al., 2016 ; Cao et al. 2018
Die-off (Eq. S10 and S27)	$f_H(T_H; 0.129, 25)$	Field experiments; Silinski et al., 2016
	$f_H(T_H; 0.019, -31)$	
	$f_H(\Delta b_-; 0.02 \text{ m}, 6.32)$ $f_H(\bar{\tau}_b^i; 0.2 \text{ N m}^{-2}, 15)$	Bouma et al., 2016 ; Cao et al. 2018 Flume experiments; calibration
Annual die-off (Eq. S11)	$P_1^{ann} = 0.5$	Calibration
<i>Scirpus maritimus</i> (species 2, middle marsh)		
Establishment (Eq. S8)	$P_2^{est} = 10^{-5}$	Calibration
	$f_B(T_H; 0.011, 0.105)$	Field experiments; Silinski et al., 2016
	$f_H(\Delta b_+; 0.03 \text{ m}, -2.37)$ $f_H(\Delta b_-; 0.001 \text{ m}, -4)$	Bouma et al., 2016 ; Cao et al. 2018
Die-off (Eq. S10 and S27)	$f_H(T_H; 0.38, 40)$	Field experiments; Silinski et al., 2016
	$f_H(T_H; 0.001, -41)$	
	$f_H(\Delta b_-; 0.075 \text{ m}, 4)$ $f_H(\bar{\tau}_b^i; 0.15 \text{ N m}^{-2}, 15)$	Bouma et al., 2016 ; Cao et al. 2018 Flume experiments; calibration
Lateral expansion	$R_2^{exp} = 2.25 \text{ m/yr}$	Remote sensing; Silinski et al., 2016
<i>Phragmites australis</i> (species 3, high marsh)		
Establishment (Eq. S8)	$P_3^{est} = 5 \times 10^{-7}$	Calibration
	$f_H(T_H; 0.035, -8.5)$	Field experiments; Silinski et al., 2016
	$f_H(\Delta b_+; 0.03 \text{ m}, -2.37)$ $f_H(\Delta b_-; 0.001 \text{ m}, -4)$	Bouma et al., 2016 ; Cao et al. 2018
Succession (Eq. S9) (from <i>Scirpus maritimus</i>)	$P_{2,3}^{suc} = 2.5 \times 10^{-6}$	Calibration
	$f_H(T_H; 0.054, -6.5)$	Field experiments; Silinski et al., 2016
	$f_H(\Delta b_+; 0.03 \text{ m}, -2.37)$ $f_H(\Delta b_-; 0.001 \text{ m}, -4)$	Bouma et al., 2016 ; Cao et al. 2018
Die-off (Eq. S10 and S27)	$f_H(T_H; 0.13, 20)$	Field experiments; Silinski et al., 2016
	$f_H(\Delta b_-; 0.1 \text{ m}, 6.32)$	Bouma et al., 2016 ; Cao et al. 2018
	$f_H(\bar{\tau}_b^i; 0.12 \text{ N m}^{-2}, 15)$	Flume experiments; calibration
Lateral expansion	$R_3^{exp} = 2.25 \text{ m/yr}$	Remote sensing; Silinski et al., 2016

Table S5: Vegetation module parameterizations (instantaneous colonization, used in reference model scenario variant).

Process	Contribution	Reference
<i>Aster tripolium</i> (species 1, pioneer marsh)		
Establishment (Eq. S8)	$p_1^{est} = \begin{cases} 1 & \text{if } H < 0.1134 \\ 0 & \text{if } H \geq 0.1134 \end{cases}$	Field experiments; Silinski et al., 2016
Die-off (Eq. S10)	$p_1^{die} = \begin{cases} 0 & \text{if } H < 0.129 \\ 1 & \text{if } H \geq 0.129 \end{cases}$	
<i>Scirpus maritimus</i> (species 2, middle marsh)		
Succession (Eq. S9) (from <i>Aster tripolium</i>)	$p_{1,2}^{suc} = \begin{cases} 1 & \text{if } H < 0.078 \\ 0 & \text{if } H \geq 0.078 \end{cases}$	Field experiments; Silinski et al., 2016
Die-off (Eq. S10)	$p_2^{die} = \begin{cases} 0 & \text{if } H < 0.38 \\ 1 & \text{if } H \geq 0.38 \end{cases}$	
<i>Phragmites australis</i> (species 3, high marsh)		
Succession (Eq. S9) (from <i>Scirpus maritimus</i>)	$p_{2,3}^{suc} = \begin{cases} 1 & \text{if } H < 0.044 \\ 0 & \text{if } H \geq 0.044 \end{cases}$	Field experiments; Silinski et al., 2016
Die-off (Eq. S10)	$p_3^{die} = \begin{cases} 0 & \text{if } H < 0.13 \\ 1 & \text{if } H \geq 0.13 \end{cases}$	

S2 Sediment accretion on vegetated platforms

Based on digital elevation maps derived from historical topographic surveys in the adjacent marshes of the Drowned Land of Saeftinghe ([Fig. 2c](#)) between 1931 and 1963 ([Wang and Temmerman, 2013](#)), we have developed an empirical relationship between mean elevation change on vegetated platforms and mean high-water depth ([Vandenbruwaene et al., 2014](#)). Here, we develop a similar relationship based on model results in the restored tidal marsh, using the same variables over the same time interval (i.e., between years 18 and 50 after de-embankment), and we compare it with the empirical relationship derived from observations.

The digital elevation maps derived from historical topographic surveys have a resolution of 20 m. To focus on vegetated platforms and avoid the influence of tidal channels, we only consider vegetated areas that are at least 200 m from tidal channels in the digital maps ([Vandenbruwaene et al., 2014](#)). Similarly, as our model results have a resolution of 5 m, we only consider areas that are at least 50 m from tidal channels in the model results.

The Drowned of Saeftinghe is located downstream of the study site, where the sediment input from the Scheldt Estuary is substantially lower. Historical measurements in the period 2001-2012 reveal that the tide-averaged SSC in the estuary is 42 mg l^{-1} close to the Drowned of Saeftinghe and 63 mg l^{-1} close the study site (Vandenbruwaene et al., 2014). To account for this 1.5 ratio in sediment input between model and observations, we multiply the observed mean elevation change by 1.5 to obtain the data presented in Fig. S1.

S3 Pioneer vegetation development

We compare our model results with observed rate of spatial expansion of the vegetation cover in the adjacent restored marshes of Paardenschor (Fig. 2c), from the onset of vegetation in 2007 until 2017. We use a series of Google Earth images, and we apply the method of Richardson et al. (2009) to classify vegetation pixels. Part of the vegetation colonization in Paardenschor starts from the dikes. Such phenomenon is expected to be of a much lesser influence in our study site. Hedwige-Prosper Polder is about 30 times larger than Paardenschor, hence the average distance to dikes will be much higher. In our analysis, we therefore remove the vegetation development occurring from the dikes.

S4 Channel network characteristics

We compare various geometric properties of the simulated tidal channels with observations in the adjacent marshes of the Drowned Land of Saeftinghe (Fig. 2c – Vandenbruwaene et al., 2013, 2015). To that end, we have developed a quasi-automatic methodology to extract tidal channel networks and related characteristics from model results. We first identify grid nodes within channels by applying a multi-window median neighborhood analysis (Liu et al., 2015) on the simulated topography, and we compute the unchanneled flow length as the shortest distance to a channel grid node (Tucker et al., 2001). We then retrieve channel edges as multiple polygons by applying the Python function `tricontour` from the visualization library `Matplotlib` (Hunter, 2007) on the channel grid nodes. We finally extract the channel network skeleton, defined as the channel centerlines (Fagherazzi et al., 1999), by generating the raw Voronoi diagram of the channel edge polygons (with the Python library `Centerline`) and applying straightforward threshold rules to simplify it.

We use a virtual topography method to determine the watershed areas along the network skeleton (Vandenbruwaene et al., 2013, 2015). In terrestrial river networks, watershed areas are exclusively delineated by topographic gradients. For tidal channel networks, however, topographic gradients are small and water flow is mainly determined by water surface gradients (Rinaldo et al., 1999). Alternatively, algorithms designed for terrestrial river networks (here the Python library `pysheds`) can be applied on a virtual topography built as the sum of the shortest distance to the network skeleton and the distance to the mouth along the network skeleton. For every point along the network skeleton, we can then compute the watershed area and the upstream mainstream length, defined as the longest upstream channel within the corresponding watershed.

Cross-sectional dimensions of tidal channels are traditionally related to the spring tidal prism (D'Alpaos et al., 2010). For tidal marsh channels, however, overmarsh tides that overtop the intertidal platform are more relevant (Vandenbruwaene et al., 2013, 2015) because maximum channel flow velocities typically occur when the surrounding platform is flooded and drained (Bayliss-Smith et al., 1979; Pethick, 1980; French and Stoddart, 1992). Here we use the mean overmarsh tidal prism, defined as the mean tidal prism from all overmarsh tides. For every point along the network skeleton, we compute the mean platform elevation of the corresponding watershed. The mean overmarsh tidal prism is then simply the product between the watershed area and the mean overmarsh high-water depth, obtained from all simulated high tides higher than the mean platform elevation.

We generate channel cross-sections along the network skeleton by balancing two constraints: cross-sections must be as perpendicular as possible to the network skeleton and consecutive cross-sections must not intersect each other. Where both constraints can be met, we then compute the channel depth as the difference between the mean channel edge elevation and the lowest cross-section elevation, the channel width as the distance between channel edges, and the cross-section area as the integral of the difference between the mean channel edge elevation and the cross-section elevation.

Additional references

Adams, M. P., Hovey, R. K., Hipsey, M. R., Bruce, L. C., Ghisalberti, M., Lowe, R. J., Gruber, R. K., Ruiz-Montoya, L., Maxwell, P. S., Callaghan, D. P., Kendrick, G. A., and O'Brien, K. R.:

- Feedback between sediment and light for seagrass: Where is it important? *Limnol. Oceanogr.*, 61, 1937-1955, <https://doi.org/10.1002/lno.10319>, 2016.
- Bayliss-Smith, T.P., Healey, R., Lailey, R., Spencer, T., and Stoddart, D.R.: Tidal flows in salt marsh creeks, *Estuar. Coast. Shelf S.*, 9, 235-255, [https://doi.org/10.1016/0302-3524\(79\)90038-0](https://doi.org/10.1016/0302-3524(79)90038-0), 1979.
- Brückner, M. Z. M., Braat, L., Schwarz, C., and Kleinhans, M. G.: What came first, mud or biostabilizers? Elucidating interacting effects in a coupled model of mud, saltmarsh, microphytobenthos, and estuarine morphology, *Water Resour. Res.*, 56, e2019WR026945, <https://doi.org/10.1029/2019WR026945>, 2020.
- Bryan, K. R., Nardin, W., Mullarney, J. C., and Fagherazzi, S.: The role of cross-shore tidal dynamics in controlling intertidal sediment exchange in mangroves in Cù Lao Dung, Vietnam, *Cont. Shelf Res.*, 147, 128-143, <https://doi.org/10.1016/j.csr.2017.06.014>, 2017.
- D'Alpaos, A., Lio, C.D., and Marani, M.: Biogeomorphology of tidal landforms: Physical and biological processes shaping the tidal landscape, *Ecohydrology*, 5, 550-562, <https://doi.org/10.1002/eco.279>, 2012.
- French, J.R. and Stoddart, D.R.: Hydrodynamics of salt marsh creek systems: Implications for marsh morphological development and material exchange, *Earth Surf. Proc. Land.*, 17, 235-252, <https://doi.org/10.1002/esp.3290170304>, 1992.
- Gourgue, O., van Belzen, J., Schwarz, C., Bouma, T.J., van de Koppel, J., and Temmerman, S.: A new bio-geomorphic model approach accounting for subgrid-scale heterogeneity of biogenic structures, *Geophysical Research Abstracts*, 21, EGU2019-16933, 2019.
- Hunter, J.D.: Matplotlib: A 2D graphics environment, *Comput. Sci. Eng.*, 9, 90-95, <https://doi.org/10.1109/MCSE.2007.55>, 2007.
- Liu, Y., Zhou, M., Zhao, S., Zhan, W., Yang, K., and Li, M.: Automated extraction of tidal creeks from airborne laser altimetry data, *J. Hydrol.*, 527, 1006-1020, <https://doi.org/10.1016/j.jhydrol.2015.05.058>, 2015.

- Marani, M., D'Alpaos, A., Lanzoni, S., Carniello, L., and Rinaldo, A.: Biologically-controlled multiple equilibria of tidal landforms and the fate of the Venice lagoon, *Geophys. Res. Lett.*, 34, L11402, <https://doi.org/10.1029/2007gl030178>, 2007.
- Mariotti, G: Marsh channel morphological response to sea level rise and sediment supply, *Estuar. Coast. Shelf S.*, 209, 89-101, <https://doi.org/10.1016/j.ecss.2018.05.016>, 2018.
- Maximova, T., Vanlede, J., Plancke, Y., Verwaest, T., and Mostaert, F.: Inrichtingsplan Hedwige-Prosperpolder: Deelrapport 1 – Numeriek 2D model, WL Rapporten, 13_166, Flanders Hydraulics Research, Antwerp, Belgium, 2014.
- Pethick, J.S.: Velocity surges and asymmetry in tidal channels, *Estuar. Coast. Shelf S.*, 11, 331-345, [https://doi.org/10.1016/S0302-3524\(80\)80087-9](https://doi.org/10.1016/S0302-3524(80)80087-9), 1980.
- Richardson, A.D., Braswell, B.H., Hollinger, D.Y., Jenkins, J.P., and Ollinger, S.V.: Near-surface remote sensing of spatial and temporal variation in canopy phenology, *Ecol. Appl.*, 19, 1417-1428, <https://doi.org/10.1890/08-2022.1>, 2009.
- Rinaldo, A., Fagherazzi, S., Lanzoni, S., Marani, M., and Dietrich, W.E.: Tidal networks: 2. Watershed delineation and comparative network morphology, *Water Resour. Res.*, 35, 3905-3917, <https://doi.org/10.1029/1999wr900237>, 1999.
- Sanford, L.P., Halka, J.P.: Assessing the paradigm of mutually exclusive erosion and deposition of mud, with examples from upper Chesapeake Bay, *Mar. Geol.*, 114, 37-57, [https://doi.org/10.1016/0025-3227\(93\)90038-W](https://doi.org/10.1016/0025-3227(93)90038-W), 1993.
- Silinski, A., van Belzen, J., Fransen, E., Bouma, T.J., Troch, P., Meire, P., Temmerman, S.: Quantifying critical conditions for seaward expansion of tidal marshes: A transplantation experiment, *Estuar. Coast. Shelf S.*, 169, 227-237, <https://doi.org/10.1016/j.ecss.2015.12.012>, 2016.
- Van de Broek, M., Vandendriessche, C., Poppelmonde, D., Merckx, R., Temmerman, S., and Govers, G.: Long-term organic carbon sequestration in tidal marsh sediments is dominated by old-aged allochthonous inputs in a macrotidal estuary, *Global Change Biol.*, 24, 2498-2512, <https://doi.org/10.1111/gcb.14089>, 2018.

- Vandenbruwaene, W., Vanlede, J., Plancke, Y., Verwaest, T., and Mostaert, F.:
Inrichtingsplan Hedwige-Prosperpolder: Deelrapport 3 – Empirisch ophogingsmodel, WL
Rapporten, 13_166, Flanders Hydraulics Research, Antwerp, Belgium, 2014.
- van Leussen, W.: The variability of settling velocities of suspended fine-grained sediment in
the Ems estuary, *J. Sea Res.*, 41, 109-118, [https://doi.org/10.1016/s1385-1101\(98\)00046-
x](https://doi.org/10.1016/s1385-1101(98)00046-x), 1999.
- Winterwerp, J.C.: On the sedimentation rate of cohesive sediment, *Proceed. Marine Sci.*, 8,
209-226, [https://doi.org/10.1016/S1568-2692\(07\)80014-3](https://doi.org/10.1016/S1568-2692(07)80014-3), 2007.
- Zhang, X., Leonardi, N., Donatelli, C., and Fagherazzi, S.: Fate of cohesive sediments in a
marsh-dominated estuary, *Adv. Water Resour.*, 125, 32-40,
<https://doi.org/10.1016/j.advwatres.2019.01.003>, 2019.
- Zhou, Z., van der Wegen, M., Jagers, B., and Coco, G.: Modelling the role of self-weight
consolidation on the morphodynamics of accretional mudflats, *Environ. Modell. Softw.*,
76, 167-181. <https://doi.org/10.1016/j.envsoft.2015.11.002>, 2016.